Cancer Nanotechnology

RESEARCH Open Access

An intelligent and self-assembled nanoscale metal organic framework (^{99m}TC-DOX loaded Fe_3O_4@Fe^{III}-tannic acid) for tumor targeted chemo/chemodynamic theranostics

Mohamed M. Swidan[1*], Nehal S. Wahba[2] and Tamer M. Sakr[3]

*Correspondence:
dr_swidan@yahoo.com

[1] Department Labeled Compounds, Hot Labs Center, Egyptian Atomic Energy Authority, PO13759, Cairo, Egypt
[2] Department of Pharmacology and Toxicology, Faculty of Pharmacy, Zagazig University, Zagazig, Egypt
[3] Radioactive Isotopes and Generators Department, Hot Labs Center, Egyptian Atomic Energy Authority, PO13759, Cairo, Egypt

Abstract

Background: Recent advances in clinical transformation research have focused on chemodynamic theranostics as an emerging strategy for tackling cancer. Nevertheless, its effectiveness is hampered by the tumor's glutathione antioxidant effect, poor acidic tumor microenvironment (TME) and inadequate endogenous H_2O_2. Hence, we designed an activatable theranostics (^{99m}Tc-DOX loaded AA-Fe_3O_4@Fe^{III}-TA) that effectively boost the catalytic efficiency of the Fenton-reaction-induced ROS production and augment the chemotherapeutic efficacy combined with diagnostic action.

Results: A cross-linked matrix of tannic acid-ferric salt (Fe^{III}-TA) as a pH-responsive shell onto ascorbic acid-decorated iron-oxide nanoparticles (AA-Fe_3O_4NPs) was prepared demonstrating a metal–organic- framework (MOF) nanostructure, followed by loading of ^{99m}Tc-labelled DOX. The platform (^{99m}Tc-DOX loaded AA-Fe_3O_4@Fe^{III}-TA) displayed suitable physical–chemical properties, including 69.8 nm particle size, 94.8 nm hydrodynamic size, − 21 mV zeta potential, effective Fe^{III}-TA shell crosslinking onto AA-Fe_3O_4NPs and 94% loading efficiency for ^{99m}Tc-DOX. The results of the *in-vitro* release investigations showed that the platform exhibited a pH-dependent release manner with 98.3% of the ^{99m}Tc-DOX being released at pH 5 (simulating the tumor's pH) and only 10% being released at the physiological pH (pH 7.4). This indicates that there was negligible payload leakage into the systemic circulation during the platform's passive accumulation inside tumor. Due to the acidic TME nature, the MOF shell might be degraded releasing free Fe^{III}, TA and a sustained release of ^{99m}Tc-DOX. Besides its chemotherapeutic impact and capacity to raise intracellular H_2O_2 content, the released ^{99m}Tc-DOX might be used as SPECT imaging tracer for concurrent tumor diagnosis. Furthermore, the mild acidity of the tumor may be overcome by the released TA, which might raise the acidification level of cancer cells. The released Fe^{III}, TA and the endogenous GSH could engage in a redox reaction that depletes GSH and reduces Fe^{III} to Fe^{II} ions which subsequently catalyze the elevated concentration of H_2O_2 to reactive •OH via Fenton-like reaction, increasing the effectiveness of chemodynamic therapy. Moreover, the *in-vivo* evaluation in tumor-bearing mice showed significant radioactivity accumulation in the tumor lesion (16.8%ID/g at 1 h post-injection) with a potential target/non-target ratio of 8.

Conclusions: The ^{99m}Tc-DOX loaded AA-Fe_3O_4@Fe^{III}-TA could be introduced as an effective chemo/chemodynamic theranostics.

Keywords: Reactive oxygen species, Chemodynamic theranostics, Fenton reaction, Controlled release, Metal–organic framework

Graphical Abstract

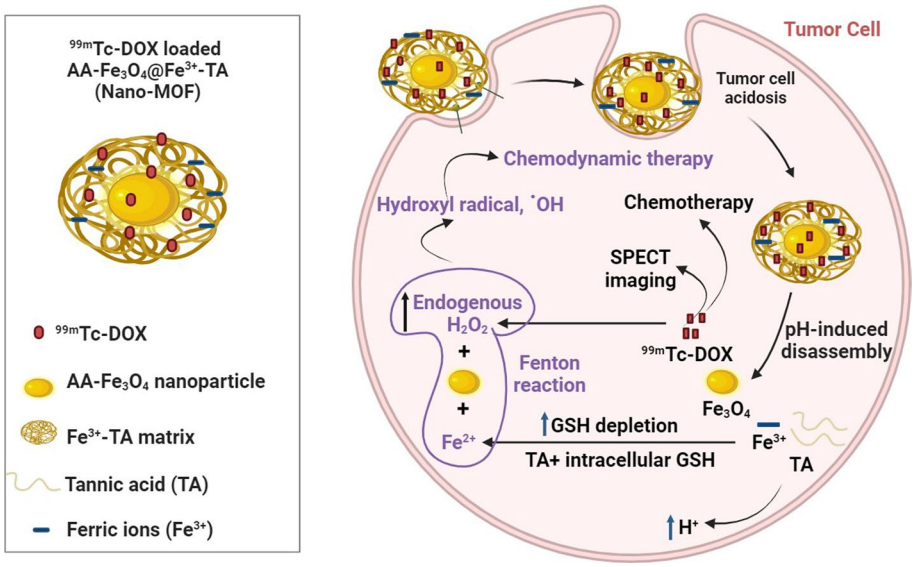

Background

Worldwide, the prevalence and death rate of cancer are on the rise and the disease represents one of the leading causes of death. Chemotherapy (CT) is an essential therapeutic practice used to treat cancer. Doxorubicin (DOX) exhibits good clinical effectiveness as an anthracycline anticancer drug, effectively treating a wide range of tumors that acts on cancer cells via intercalating into DNA and interfering with topoisomerase-II-mediated DNA repair. Moreover, it may increase the intracellular hydrogen peroxide (H_2O_2) levels by activating poly-ADP ribose polymerase (PARP) and nicotinamide adenine dinucleotide phosphate hydrogen (NADPH) oxidase posing enhanced oxidative stress (Thorn et al. 2011; Mizutani et al. 2005; Deng et al. 2007). Despite being widely used in medicine, DOX has been demonstrated to have a variety of dangerous side effects including hepatotoxicity, cardiotoxicity, neurotoxicity and nephrotoxicity (Ajaykumar 2020).

Recently, chemodynamic theranostic (CDT) has been perceived as an emerging and effective approach to cancer management. It is based on the fact that in the tumor microenvironment (TME), Fenton or Fenton-like agents catalyze the in-situ conversion of H_2O_2 to very dangerous reactive oxygen species (ROS) (Tang et al. 2019; Wang et al. 2020a; Lin et al. 2019). CDT has numerous distinct advantages over traditional cancer treatment strategies, among them the capacity to regulate the TME, significant tumor specificity, regression and penetration, endogenous stimulus activation and reduced

off-target concerns (Lin et al. 2018; Liu et al. 2020a; An et al. 2020; Ding et al. 2019). Additionally, it is more suited for treating deep tumors as it doesn't require external stimulation as sound or light, unlike sonodynamic therapy and photodynamic therapy (Cui et al. 2021; Shi et al. 2021). Unfortunately, CDT is encountering certain hurdles due to inadequate concentration of endogenous H_2O_2, insufficient acidity and a glutathione (GSH)-rich antioxidant system in TME (Liu et al. 2018; Gu et al. 2020; Han et al. 2019). Despite substantial advances via employing inorganic nano-catalytic processes including metal ions-induced Fenton-like reactions (Ce^{3+}, Cu^{2+}, Co^{2+} and Mn^{2+}), these CDT agents are bound to confront biosafety concerns due to their high toxicity (Wang et al. 2019; Ma et al. 2018; Gao et al. 2019; Nie et al. 2020). In addition, the adoption of H_2O_2 generators such as glucose oxidase (GOX) and calcium peroxide (CaO_2) nanoparticles encountered a major obstacle related to the quick burst release of H_2O_2 during its generation process, which prevented it from being completely utilized in practice (Cui et al. 2021; Huang et al. 2021; Liu et al. 2020b). In recent times, GOX has been incorporated into nano-sized metal–organic framework (nano-MOF) or coupled with Fe_3O_4 NPs, which are iron-based nanomaterials with good biosafety profile (Zheng et al. 2023; Feng et al. 2019). Through this process, GOX can convert glucose into gluconic acid, improving the acidic levels of tumors and enhancing Fenton-like reactions by increasing the generation of hydroxyl radicals (•OH). Furthermore, additional tactics like carbonic anhydride IX inhibition or siRNA silencing may also quicken the Fenton reaction of Fe_3O_4 by raising the tumor's acidity level (Liu et al. 2018; Chen et al. 2020). However, throughout the blood circulation process, the unregulated reaction between GOX and glucose may result in "off-target" adverse effects for healthy tissues (Ding et al. 2020). Consequently, a great deal of work has been conducted to develop a variety of highly effective CDT strategies for treating cancer. The combined approach of CT with CDT may significantly increase the efficacy of cancer treatment because CDT increases the tumor suppressor effect of CT by upsetting both TME and tumor physiology (Wang et al. 2021a; Lei et al. 2021). MIL-101(Fe)-NH_2 nanoscale MOF demonstrated high DOX loading efficiency, pH-responsive release property, enhanced tumor cell uptake and efficient chemodynamic activity (Wang et al. 2015). In addition, Honghui Li et *al*. successfully prepared a pH-responsive iron-based MOF (MTD) that showed an effective concentration of DOX, elevated intracellular H_2O_2 concentration at the tumor site and high therapeutic efficacy based Fenton reaction (Li et al. 2022). The majority of synergistic therapy-based drug delivery systems (DDSs) are sophisticated since they incorporate numerous diverse features. It is therefore crucial to determine the best strategy for integrating CT and CDT to produce multifunctional DDSs.

With the aforementioned issues in consideration, herein, we designed an activatable nanotheranostics (^{99m}Tc-DOX loaded AA-Fe_3O_4@Fe^{III}-tannic acid) affording pH-dependent spatiotemporal DOX release, H_2O_2 self-supply and GSH depletion for effective tumor growth suppression. The platform was constructed in a core–shell MOF-structure where a cross-linked matrix of Fe^{III}-TA served as a pH-responsive shell on the surface of AA-Fe_3O_4 NPs, followed by loading of technetium-99m [^{99m}Tc]-labeled DOX. Interestingly, the biocompatible and biodegradable platform had the ability to accumulate passively inside tumors with little payload leakage in the systemic circulation because of the MOF shell's protective function. Following the platform's entry into tumor

cells, the acidic properties of TME may cause the MOF shell to break down, releasing free Fe^{III}, TA and sustained release of ^{99m}Tc-DOX. In addition to its chemotherapeutic and imaging properties, ^{99m}Tc-DOX could increase the intracellular H_2O_2 concentration. The liberated TA might be able to increase the acidification level of cancer cells overcoming the tumor's modest acidity. Crucially, both TA and GSH might quickly convert the liberated Fe^{III} to ferrous ions (Fe^{II}), increasing GSH depletion. The generated Fe^{II} ions along with the elevated level of intracellular H_2O_2 might be effectively transformed into extremely reactive $^{\bullet}OH$ via the Fenton reaction. Lastly, the ready platform may offer a different approach to combine CT and CDT to generate effective theranostics.

Experimental section

Chemicals and materials

All chemicals, unless noted differently, were delivered in analytical grade form and used right away without additional purification. Ferrous chloride tetrahydrate, 99% ($FeCl_2.4H_2O$, M.Wt. 198.81 g/mol), ferric chloride hexahydrate, 99% ($FeCl_3.6H_2O$, M.Wt. 270.33 g/mol), aqueous ammonia, 99,9% (NH_4OH, M.Wt. 35.05 g/mol), Acetone, 99.9% (CH_3COCH_3, M.Wt. 85.08 g/mol), L-Ascorbic acid, 99%, ($C_6H_8O_6$, M.Wt.176.12 g/mol), tannic acid, ($C_{76}H_{52}O_{46}$, M.Wt. 1701.20 g/mol), Hydrogen peroxide, 30% (H_2O_2, M.Wt. 34.01 g/mol), methylene blue ($C_{16}H_{18}ClN_3S$, M.Wt. 319.85 g/mol), 2',7'-dichlorofluorescin diacetate (DCFH-DA), 97% ($C_{24}H_{16}Cl_2O_7$, M.Wt. 487.29 g/mol), doxorubicin hydrochloride, 98% ($C_{27}H_{29}NO_{11}$·HCl. M.Wt. 579.98 g/mol) and Whatman paper No.1 sheets were obtained from Sigma Aldrich company, St. Louis, Mo., USA. A planed, round neodymium magnet (diameter 10 mm, capacity 100 mT) was applied from Ningbo Daxie Magnetic Co., Ltd., China. The radioactive material (^{99}Mo/^{99m}Tc generator) was gifted by the Radioisotopes Production Facility (RPF), Egyptian Atomic Energy Authority (EAEA).

Equipment and characterizations

Transmission electron microscopy (TEM; JEM-1230; JEOL, Tokyo, Japan) was conducted with 200 kV accelerating voltage for the determination of the particles size. Dynamic light scattering (DLS; Zetasizer Nano-system Nano-ZS90, Malvern, UK) was utilized for hydrodynamic size and zeta potential determination. Fourier transform infrared (FTIR; VERTEX 70; Bruker, Bremen, Germany) was performed to investigate the composition of the as-prepared nanoparticles. UV–vis spectrophotometer (U-4100, Japan) was applied to investigate the UV–vis absorption spectra. A NaI (Tl) γ-ray scintillation counter (Scaler Ratemeter SR7 model, UK) was applied for radioactivity determination.

Methods

Preparation of ascorbic acid-coated *iron* oxide nanoparticles (AA-Fe_3O_4 NPs)

The synthesis of AA-Fe_3O_4 NPs was performed according to previous literatures with some modifications (Shagholani and Ghoreishi 2017; Swidan et al. 2022). Briefly, ferrous and ferric salts in molar ratio 1:2 were dissolved in 40 ml oxygen-free bi-distilled water before the temperature was gradually raised to 50 C in a nitrogen environment with steady stirring for 0.5 h. Then, the ammonia solution was added dropwise till pH

10 which was then maintained at that pH and temperature for an additional 0.5 h. The aforesaid reaction mixture was then supplied with a 20 mL addition of 10% AA (aqueous solution). The reaction took place for 1 h with constant stirring at 50 °C to functionalize the particles with AA. The obtained black precipitate (AA-Fe_3O_4 NPs) was extracted from the separated solution by magnetic decantation and repeatedly washed with bi-distilled water to bring a neutral pH for further study.

Preparation of nanoscale metal–organic framework (AA-Fe_3O_4@Fe^{III}-Tannic acid)

Tannic acid (TA) solution (40 mg/mL) was slowly added to the prepared solution of AA-Fe_3O_4 NPs (10 mg/mL) in which the mixture was mechanically stirred for 2 h. Then, 10 mL solution of $FeCl_3.6H_2O$ (10 mg/mL) was added while the pH ~ 7.4 was adjusted using HEPES buffer and the mechanical stirring was employed for another 2 h to facilitate the complexation reaction between TA and the metal ions (Fe^{III}) (Ejima et al. 2013). Finally, the obtained nanoscale MOF (AA-Fe_3O_4@Fe^{III}-TA) was separated utilizing magnet, washed many times and dried under vacuum.

Drug loading and release studies

A definite volume of an aqueous drug solution (DOX.HCl, 1 mg/mL) was ultrasonically dispersed in an aqueous solution (5 mg/mL) of the nano-MOF in which the final mixture was mechanically stirred at ambient temperature for 6 h. Thereafter, DOX-loaded nano-MOF (DOX-loaded Fe_3O_4@Fe^{III}-TA) was separated from the solution at different time intervals by a magnet in which the supernatant was utilized to determine the unloaded DOX via spectrophotometric analysis at 480 nm. The drug loading efficiency and capacity were estimated by the following formulas:

$$\text{Loading efficiency } \% = \frac{\text{Total DOX} - \text{unloaded DOX}}{\text{Total DOX}} \times 100 \quad (1)$$

$$\text{Loading efficiency } (\mu g/\text{mg}) = \frac{\text{Total DOX} - \text{unloaded DOX}}{\text{Wt. of nano} - \text{MOF}} \times 100 \quad (2)$$

The pH-triggered release study of the prepared DOX-loaded nano-MOF was conducted in phosphate-buffered saline (PBS) compromising pH of 7.4 and 5. Typically, 1 ml of DOX-loaded nano-MOF (1 mg/mL) was wrapped in the dialysis bag which placed within 19 mL PBS and exposed for continuous shaking at room temperature. At the scheduled intervals (0.5, 1, 2, 4, 8 h), 1 mL dialysis buffered-solution was withdrawn and retrieved for analysis using UV/vis absorption at 480 nm, before being replaced with new PBS of the same volume and pH value.

pH-dependent degradation of the nanoscale MOF (AA-Fe_3O_4@Fe^{III}-TA)

The release of Fe^{II} at various time intervals was evaluated using the 1,10- Phenanthroline colorimetric technique (Zhang et al. 2018). First, 200 µL of different concentrations of $FeCl_3$ solutions were incubated with 200 µL of ascorbic acid (1 mM) at ambient temperature for 3 min. After that, 200 µL of 1,10- Phenanthroline (1 mg/mL) was added, and after 10 min., the mixture's absorption at 510 nm was measured using a UV–vis spectrophotometer demonstrating the implementation of the calibration curve. The sample;

AA-Fe_3O_4@Fe^{III}-TA (1 mL, 5 mg/mL) was put into dialysis bags, which were then submerged in buffer solutions (19 mL) with various pH levels (pH 7.4 and 5). A sample of the dialysis buffer (200 µL) was taken and new buffer (200 µL) was introduced at various intervals (0–8 h). After 10 min reaction with 1,10-phenanthroline, the released Fe^{II} content was determined by measuring the absorbance at 510 nm of the withdrawn solution using a UV–vis spectrometer.

In-vitro Fenton-like reaction of the nanoscale MOF

The chemodynamic activity was investigated as follow (Guo et al. 2019; Guo et al. 2020): nano-MOF was incubated with 400 µl PBS (pH 5) containing methylene blue (MB; 0.1 M) and hydrogen peroxide (8 mM). After 1 h of incubation at 37 °C, the change in the absorbance value at 665 nm was used to track the hydroxyl radical (•OH)-induced MB degradation. For control experiment, the exact concentrations of MB and a mixed solution of H_2O_2/MB as those of the aforementioned sample were also analyzed similarly.

In-vitro anticancer efficacy determination

Cell culture

The human breast cancer cells (MCF-7) were acquired from the VACSERA tissue culture unit (Giza, Egypt). They were cultivated in Dulbecco's modified Eagle's medium (DMEM) that contained gentamycin (1%), 10% fetal bovine serum (FBS) and L-glutamine. The cultures were maintained for 7 days at 37 C in a humid environment with 5% CO_2.

Cell viability assay

The 3-(4, 5-dimethylthiazol-2-yl)-2,5-diphenyltetrazolium bromide (MTT) assay was used to examine the cell viability. In a 96-well plate, MCF-7 cells were sown and grown for 24 h at 37 °C in 100 µL of DMEM medium. The medium was then swapped out for 200 µL of new media that included various concentrations of DOX, nano-MOF or DOX-loaded nano-MOF. The control cell line was assessed without using any of the tested samples. MTT (20 µL, 5 mg/mL) was then added and incubated for a further 24 h to create purple formazan. After centrifugation, an optical density microplate reader was used to track the results by contrasting the absorbance at 570 nm of treated and untreated cells.

Oxidative stress markers determination

Intracellular reactive oxygen species (ROS) determination

A 12-well plate supplemented with MCF-7 cells (6×10^4 cells/well) was left incubating for 24 h after which fresh culture medium containing DOX, nano-MOF or DOX loaded nano-MOF (IC_{50} concentration for each one) was used to replace the original medium. The culture medium was pulled out and wiped with PBS after 4 h of incubation. Each well was then filled with fresh culture medium (1 mL) containing 2,7-dichlorofluorescin diacetate (DCFH-DA; 10 µg/mL), and after 30 min of incubation, the culture medium was removed and cleaned with PBS. The cells were then centrifuged after being lysed in an alkaline solution. A microplate reader with 96-well filled with 200 µL of supernatant

was used to monitor the fluorescence at 485 nm excitation and 520 nm emission. The results were displayed as a mean of the fluorescence intensity (Fukumura et al. 2012).

Intracellular glutathione (GSH) levels determination

A set of MCF-7 cells were exposed to DOX, nano-MOF or DOX-loaded nano-MOF for 2 h. A different group received catalase (CAT) before the treatment with the prepared formulations. The cells were taken out, cleaned, and lysed in 40 µL of Triton X-100 lysis buffer on ice. Twenty minutes later, lysates centrifugation was performed in which 10 µL of the supernatant was combined with 50 µL of Ellman's reagent (0.5 mM DTNB). Using a microplate reader, the absorbance at 405 nm was measured to determine the GSH concentration (Wang et al. 2021b).

Radiochemistry

Radiolabeling of DOX with ^{99m}Tc

The radiolabeling of DOX with Tc-99m was accomplished using a simple reductive methodology (El-Ghareb et al. 2020). The radiolabeling technique was launched in which the reaction parameters including the concentration of DOX (0.25–1.5 mg/mL), stannous chloride (25–200 µg/mL), reaction time (15–60 min) and pH (3–9) were tuned to get the highest radiochemical yield % (RCY). The radiolabeling efficiency was determined by means of ascending paper chromatographic analysis (Whatman paper no. 1 strips; 13 cm length and 1 cm width), whereby acetone and saline were used as mobile phases for the detection of free pertechnetate and other radioactive impurities, respectively.

^{99m}Tc-DOX loading study

As previously stated in the non-radioactive DOX loading fashion, a set volume of ^{99m}Tc-DOX solution (1 mg/mL) was immediately dispersed with a definite volume of nano-MOF (1 mg/mL) followed by magnetic stirring for 3 h. At each predetermined time-step following magnetic decantation, the radioactivity in the precipitate (^{99m}Tc-DOX loaded nano-MOF) and the supernatant (^{99m}Tc-DOX) were measured and applied to compute the loading efficiency percent using the formula given:

$$\text{Loading efficiency\%} = \frac{\text{Radioactivity in the precipitate}}{\text{Radioactivity in the precipitate} + \text{Radioactivity in the supernatant}} \times 100 \quad (3)$$

In-vitro serum stability analysis

It is noteworthy that exploring the radiochemical procedure's tolerability in physiological settings should be investigated. In brief, a 1 mL reaction volume containing ^{99m}Tc-DOX loaded nano-MOF product (0.1 mL) and Ringer's solution (0.9 mL, pH = 7.4) or mice serum (0.9 mL) was incubated at 37 °C for 24 h. Through using paper chromatographic procedures outlined before, the radiochemical yields were recorded at various intervals of time.

In-vivo experiments

Animal models and tumor inoculation

The National Cancer Institute (Cairo, Egypt) provided the primary tumor-induced mouse (Ehrlich Ascites Carcinoma) and all healthy Swiss albino male mice with usual weights of 25–35 g ($n=60$). After the tumor in the primary mouse had formed for 5–6 days, the ascites fluids were collected and re-dispersed in 5 mL saline. For tumor inoculation, the healthy mice were subcutaneously injected in the right flank with the required volume (0.2 mL) of ascites fluids. The mice were monitored for 5–7 days until the tumor mass had fully formed and had an average volume of 1 ± 0.1 cm^3 (Korany et al. 2020). All mice, both healthy and those had developed tumors, were kept in comfortable housing with consistent dietary and environmental parameters under the supervision of a veterinarian.

Bio-distribution studies

The mice were categorized into two groups, each with 30 animals. Group (A) had included normal mice, whereas Groups (B) had included mice that had undergone tumor induction. All of the two groups' members intravenously (i.v.) received treatment with ^{99m}Tc-DOX loaded nano-MOF in the tail vein. Using a well-equipped NaI gamma counter, it was possible to quantify the accumulation of ^{99m}Tc-DOX loaded nano-MOF in various organs and tumor tissues at 0.25, 0.5, 1, 2 and 4 h after injection. Percentage Injected Dose per Gram Organ (% ID/g ± SD) was used to examine the findings of 5 mice at every interval. Moreover, a time-dependent evaluation of the target/non-target (T/NT) ratios post-injection was also performed.

Statistical analysis

The data, with respect to the control group, were averaged over three replicates unless explicitly stated. A p-value of less than 0.05 from the One-Way ANOVA test indicated a statistically significant result.

Results and discussion

Synthesis and characterizations of the nanoscale AA-Fe_3O_4@Fe^{III}-TA framework

The synthesis of AA-Fe_3O_4 NPs was made via a co-precipitation approach in which a stoichiometric mixture of ferrous and ferric salts in an aqueous environment was employed to produce Fe_3O_4 NPs. While ascorbic acid was utilized as a functionalizing (coating) agent to provide Fe_3O_4 NPs with the required stability because it is widely used as a biocompatible surfactant for superparamagnetic iron oxide nanoparticles (Özel et al. 2019; Sreeja et al. 2015; Ozel et al. 2018; Asefi et al. 2021). Subsequently, the nano-MOF (AA-Fe_3O_4@Fe^{III}-TA) with core–shell structure was fabricated by simply mixing AA-Fe_3O_4 NPs with the self-assembly TA and Fe^{III} matrix. Throughout the assembly process, TA serves as an organic ligand whereas Fe^{III} operates as an inorganic cross-linker, leading to the formation of a cross-linked Fe^{III}-TA shell on the surface of the AA-Fe_3O_4 NPs (Ejima et al. 2013).

According to TEM investigation, the produced AA-Fe_3O_4 NPs proclaimed discrete and quasi-sphered morphology, uniform particles size ~ 34.4 ± 6.1 and narrow size distribution, as shown in Fig. 1a, b. The synthesized nano-MOF (AA-Fe_3O_4@Fe^{III}-TA)

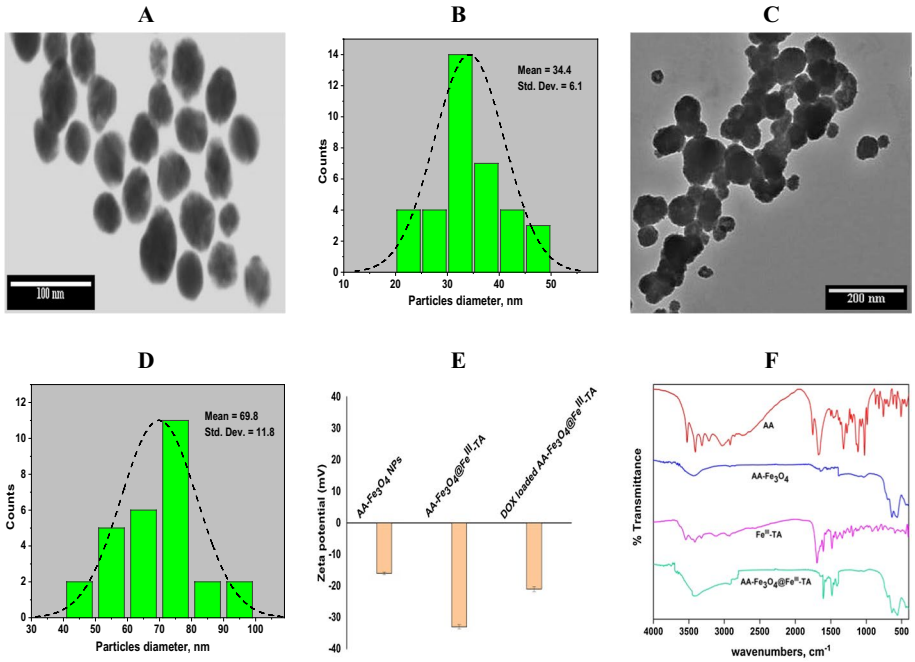

Fig. 1 Physicochemical characterization of AA-Fe_3O_4 NPs and AA-Fe_3O_4@Fe^{III}-TA. **a**–**d** The representative TEM images **a** and **c** and size distribution **b** and **d** of AA-Fe_3O_4 NPs and AA-Fe_3O_4@Fe^{III}-TA, respectively. **e** Zeta potential measurements in water. **f** FT-IR spectroscopic analysis

was further examined by TEM, which revealed that the morphology was mostly still quasi-spherical but showed somewhat agglomeration, increasing the particle size to ~ 69.8 ± 11.8 as depicted in Fig. 1c, d. Zeta potential (ζ- potential) measurements were used to exhibit the core–shell structure after proper surface engineering. Fe^{III}-TA shell caused a considerable change in the surface charge compared to the as-produced AA-Fe_3O_4 NPs (ζ- potential: from -16 mV to -33 mV; Fig. 1e), which was attributed by the availability of many hydroxyl groups in TA represented in the construction of the nano-MOF (Chen et al. 2022a). The FTIR analysis (Fig. 1f) was carried out to confirm the proper synthesis of AA-Fe_3O_4 NPs and the efficient crosslinking of Fe^{III}-TA shell onto AA-Fe_3O_4 NPs. In contrast to pure AA, the spectra of AA-Fe_3O_4 NPs showed the loss of the lactone ring's C = O band (1750 cm^{-1}), a shift in the C = C band (1665 to 1635 cm-1), and the emergence of a new stretching band for Fe–O (589 cm^{-1}). These are reliable signs that AA-Fe_3O_4 NPs successfully formed. The spectrum of AA-Fe_3O_4@Fe^{III}-TA displayed a broadband (3600–2700 cm^{-1}) indicating the numerous hydroxyl groups of polyphenols, absorption peaks (1400–1600 cm^{-1}) attributed to stretching and vibration of substituted benzene rings, as well as the distinctive band of Fe–O (589 cm^{-1}). This FTIR investigation revealed further evidence of Fe^{III}-TA coating on AA-Fe_3O_4 NPs.

Doxorubicin loading and pH triggering release studies

The nano-MOF have been widely recognized as effective nano-carriers for loading diverse compounds due to their enormous surface area (Chen et al. 2022b). The goal of this study was to load DOX onto the synthesized nano-MOF (AA-Fe_3O_4@Fe^{III}-TA). The UV/vis absorption of DOX at 480 nm was employed to track the DOX loading

utilizing the standard calibration curve (Fig. 2a). The loading efficiency and capacity were tested for the effect of stirring duration revealing the highest values (98% loading efficiency, 196 µg/mg loading capacity) at 4 h post-stirring (Fig. 2b). Such an effective DOX loading might be attributable to the electrostatic attraction between the positively charged DOX (protonated amino groups) and the negatively charged hydroxyl groups of TA (El-Ghareb et al. 2020; Chen et al. 2022b). After DOX loading, the prepared DOX-loaded nano-MOF was exposed for DLS analysis declaring that the hydrodynamic size was ~ 94.8 nm while the ζ- potential measurements exhibited – 21 mV (Figs. 2c & 1e, respectively). The reduction of ζ- potential might be due to the affordable amine groups in DOX that may partially compensate the negative charge (El-Ghareb et al. 2020).

The dialysis technique was used to examine the drug-pH-triggered release profile. Under pH 7.4 which mimics the physiological environment, the loaded DOX exhibited low release behavior with an accumulative amount ~ 10 ± 0.93% after 8 h (Fig. 2d). So, it was possible to deduce that the system could be injected steadily during blood circulation with little to no pre-leakage. On the other hand, reducing the pH to 5 (simulating the tumor environment) resulted in reasonable acceleration of DOX release in a sustained manner with an accumulative amount ~ 98.3 ± 0.97% after 8 h (Fig. 2d). This is likely due to the dissociation of Fe^{III}-TA matrix under an acidic condition (Chen et al. 2022a; Liu et al. 2019).

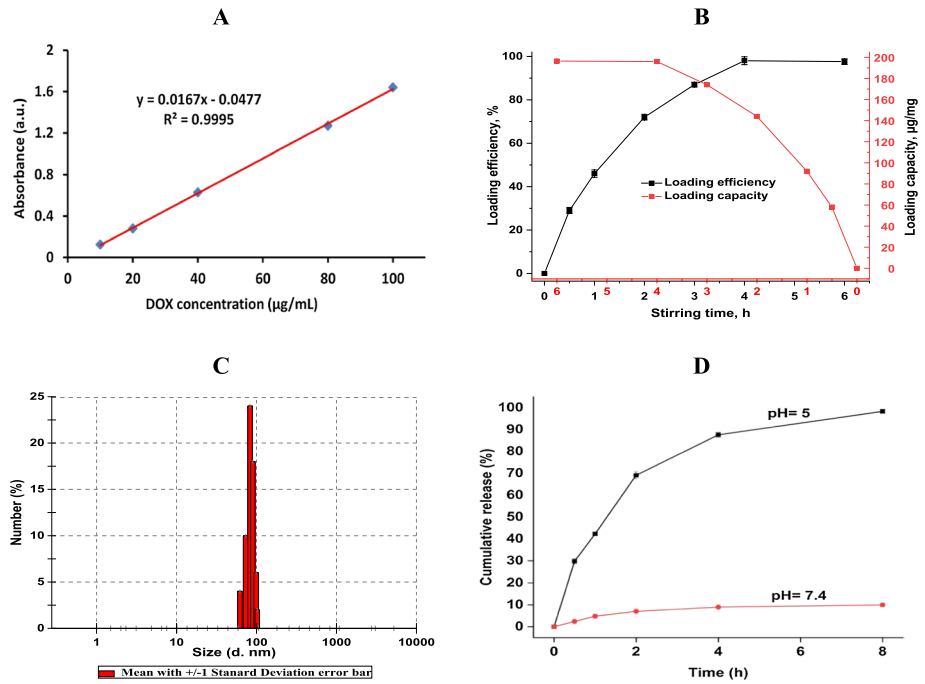

Fig. 2 Loading and release studies of DOX. **a** The calibration curve of DOX by UV/vis absorbance at 480 nm. **b** DOX loading efficiency and capacity at different stirring intervals. **c** Hydrodynamic size distribution of DOX loaded AA-Fe_3O_4@Fe^{III}-TA in aqueous medium. **d** Drug release profiles of DOX-loaded AA-Fe_3O_4@Fe^{III}-TA in PBS buffer with different pH values. Data was represented as mean ± SD ($n = 3$)

pH-dependent degradation inducing Fe^{II} release

The traditional 1,10-phenanthrene colorimetric technique was used to quantify the generation of Fe^{II}. In phosphate buffer solutions with pH values 7.4 and 5.0, the release of Fe^{II} ions from AA-Fe_3O_4@Fe^{III}-TA was monitored over time. Under neutral conditions, as shown in Fig. 3a, the released Fe^{II} concentration was extremely low. On the other hand, under mild acidic circumstances, it displayed a time-dependent release pattern that revealed the release of Fe^{II} ions with percentages of 5 ± 0.02 and 57 ± 0.03 of the initial concentration of Fe^{III} ions at 1 and 8 h after the reaction, respectively (Fig. 3a). This might be the result of the Fe^{III}-TA matrix dissociation in an acidic environment, releasing both Fe^{III} and TA (Chen et al. 2022a; Liu et al. 2019). It is important to note that naturally occurring polyphenols, such as TA, have been shown to function as reducing agents for facilitating Fe^{II} generation by accelerating the Fe^{III}/Fe^{II} conversion (Li et al. 2022; Guo et al. 2020). The foregoing findings showed that AA-Fe_3O_4@Fe^{III}-TA exhibited good acidity responsiveness and effective production of Fe^{II} to function as a Fenton reaction catalyst for producing hazardous $^{\bullet}OH$.

In-vitro Fenton-like reaction of the nanoscale MOF

The demonstration of the Fenton-like reaction ability (chemodynamic activity) of the nano-MOF (AA-Fe_3O_4@Fe^{III}-TA) in the presence of H_2O_2 under acidic conditions (simulating TME) was conducted using the MB colorimetric method (Guo et al. 2019; Guo et al. 2020). MB has a markedly UV–vis adsorption peak at 665 nm, despite that it is susceptible to being promptly degraded by $^{\bullet}OH$, triggering the disappearance of UV–vis adsorption (Guo et al. 2019; Guo et al. 2020). As seen in Fig. 3b, the absorbance of MB drastically dropped after incubation with AA-Fe_3O_4@Fe^{III}-TA and H_2O_2, whereas H_2O_2 treated alone with MB did not appear to experience any obvious drop. These results may be attributed to the ability of AA-Fe_3O_4 NPs and Fe^{III}-TA matrix to catalyze H_2O_2 in a weak acidic environment to produce $^{\bullet}OH$ efficiently (Cui et al. 2021; Chen et al. 2021; Dai et al. 2018). The acidic environment induces the dissociation of Fe^{III}-TA shell to Fe^{III}

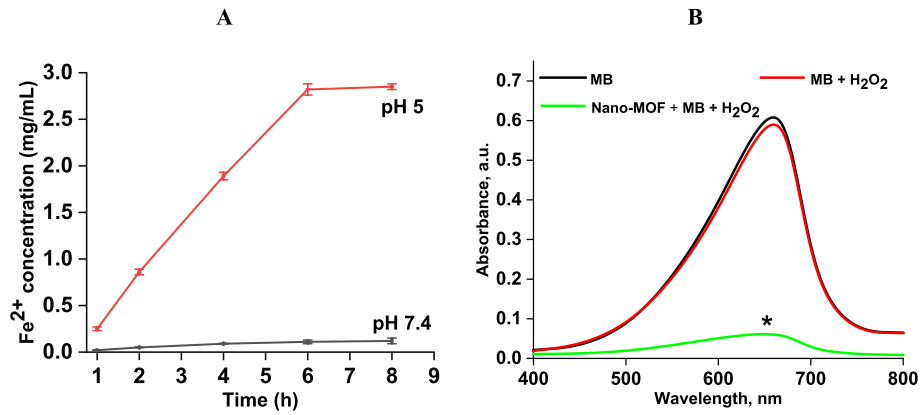

Fig. 3 In-vitro Fenton-like reaction of AA-Fe_3O_4@Fe^{III}-TA: **A** time-dependent generation of Fe^{II} ions in PBS with different pH values using 1,10-phenanthrene colorimetric method. **B** Determination of $^{\bullet}OH$ using MB colorimetric method in the presence of H_2O_2 under acidic conditions (pH 5). Data was represented as mean ± SD ($n = 3$). Means were compared using ANOVA, followed by the Tukey test for multiple comparisons, two-to-two. ($^{*}p \leq 0.05$, ($^{a}p > 0.05$)

and TA which has the ability to reduce the generated Fe^{III} to Fe^{II} inducing the degradation of H_2O_2 into highly cytotoxic $^{\bullet}OH$ via Fe^{II}-mediated Fenton-like reaction as declared by the following reaction (Liu et al. 2020a; Chen et al. 2022b):

$$Fe^{2+} + H_2O_2 \rightarrow Fe^{3+} + {}^{\cdot}OH + OH^{-} \quad (4)$$

In-vitro anticancer efficacy determination

Cell viability assay

The MTT assay was used to assess the cytotoxic activity of DOX, nano-MOF and DOX-loaded nano-MOF against the MCF-7 cell line (Fig. 4). The outcomes supported the existence of a positive correlation between the examined concentrations per each model and the cytotoxic behavior. In contrast to DOX and nano-MOF, which had IC_{50} values of 0.55 and 6.8 µg/ml, respectively, DOX-loaded nano-MOF was found to have an IC_{50} value of just 0.08 µg/ml. With regard to ~ 7 times-fold reduction in the DOX inhibitory concentration necessary to kill 50% of MCF-7 cells, the beneficial contribution of the cytotoxic carrier (DOX loaded AA-Fe_3O_4@Fe^{III}-TA) should be viewed as a synergistic effect of chemotherapy and chemodynamic therapy. The chemotherapeutic effect may be attributable to the

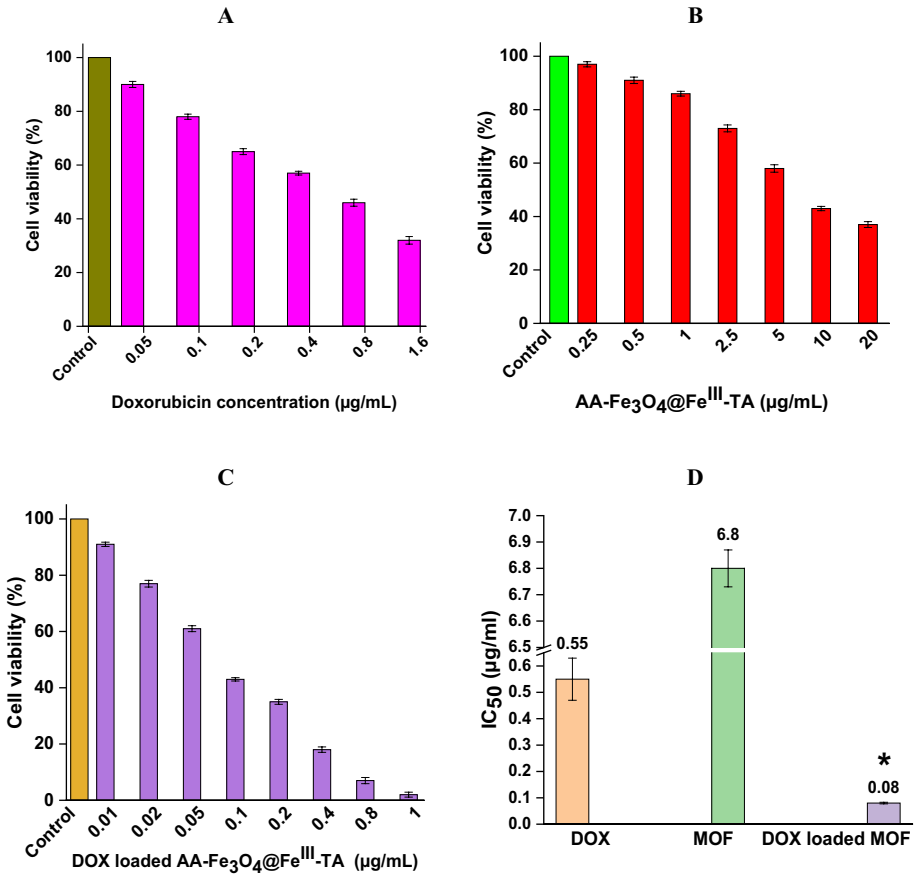

Fig. 4 The cell viability of MCF-7 cells treated with different formulations: **A** DOX **B** AA-Fe_3O_4@Fe^{III}-TA and **C** DOX loaded AA-Fe_3O_4@Fe^{III}-TA at various concentrations using MTT assay. **D** IC_{50} comparative diagram. Data was represented as mean ± SD ($n = 3$)

sustained release behavior of DOX inside the tumor cells while the chemodynamic activity may be due to the cytotoxic •OH via Fe^{II}-mediated Fenton-like reaction (Chen et al. 2022a; Chen et al. 2022b; Liu et al. 2019). These findings concurred with those who investigated how nanoparticles and their associated Fenton reaction might have the potential of an efficient synergistic approach for CT and CDT (Cui et al. 2021; Nie et al. 2020; Chen et al. 2021; Fu et al. 2021; Liang et al. 2019).

Oxidative stress markers determination

Intracellular reactive oxygen species (ROS) determination

The ROS generating ability of the prepared nano-MOF in MCF-7 cells was initially studied utilizing DCFH-DA assay kit (Fukumura et al. 2012; Li et al. 2021). As seen in Fig. 5A, the Fe^{III}-TA complex fluorescence intensity was remarkably low and similar to that of the control group. When cells were treated simply with either DOX or AA-Fe_3O_4@Fe^{III}-TA, the fluorescence intensity increased in comparison to the control (~ 5.2 or 13.5 times, respectively) indicating ROS production which may be attributed to DOX-induced oxidative stress (Hernandes et al. 2023) or the enhanced Fenton reaction of AA-Fe_3O_4@Fe^{III}-TA (Chen et al. 2021; Fu et al. 2021). While the treatment of MCF-7 cells with DOX-loaded AA-Fe_3O_4@Fe^{III}-TA augmented the fluorescence intensity by ~ 19 times compared to the control, demonstrating the synergistic effect of CDT and CT. As an added benefit, DOX could produce more H_2O_2 inside cells, which could mediate DOX cytotoxicity in species-mediated ways (Wagner et al. 2005; Ubezio and Civoli 1994). This attribution stems from the metabolic reductive activation of DOX to a semiquinone that promotes the generation of superoxide and is then dis-mutated by superoxide dismutase enzymes, resulting in the synthesis of H_2O_2 as represented in the subsequent equations:

$$\mathrm{DOX} \rightarrow \mathrm{DOX\,semiquinone}\cdot^{\sim} \tag{5}$$

$$\mathrm{DOX\,semiquinone}\cdot^{\sim} + \mathrm{O_2} \rightarrow \mathrm{DOX} + \mathrm{O_2}\cdot^{\sim} \tag{6}$$

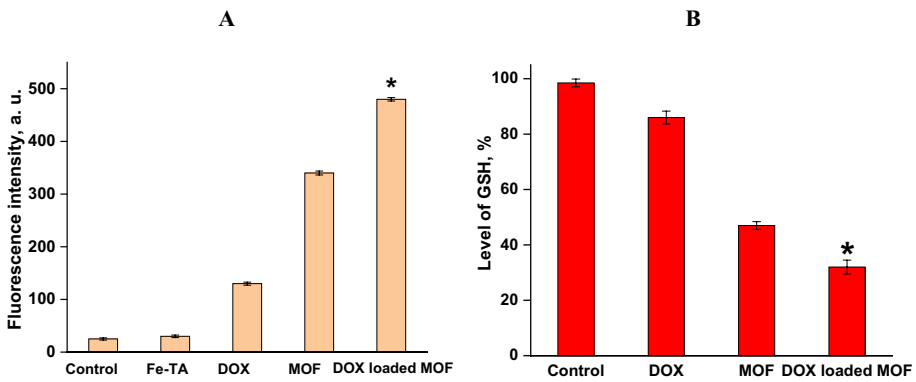

Fig. 5 Oxidative stress markers determination in MCF-7 cells treated with different formulations: **A** Quantitative analysis of the fluorescence intensity (λex/em = 485/520 nm) of DCF-induced ROS production **B** The GSH depletion activity for 0.5 h incubation. Data was represented as mean ± SD ($n = 3$). Means were compared using ANOVA, followed by the Tukey test for multiple comparisons, two-to-two. $^{*}p \leq 0.05$ is deemed a significant difference

$$O_2 \cdot^{\sim} + 2H^+ \rightarrow H_2O_2 \quad (7)$$

Intracellular glutathione (GSH) levels determination

Due to the availability of intracellular antioxidants, such as GSH, tumor cells have an increased capacity to scavenge RO;8S, which typically restricts the therapeutic efficacy of CDT. Therefore, a number of techniques have been devised to improve the CDT by decreasing intracellular GSH (Guo et al. 2019; Chen et al. 2021; Fu et al. 2021). This objective can be met in our system (DOX loaded AA-Fe_3O_4@Fe^{III}-TA) by evaluation of the GSH depletion activity as illustrated in Fig. 5B. It showed that both nano-MOF and DOX-loaded nano-MOF-treated cells had a significantly low GSH level (47 and 32%, respectively), whereas DOX-treated cells only marginally consumed the cellular GSH in an approximately similar manner of the control group. Because of AA-Fe_3O_4@Fe^{III}-TA's propensity to induce the Fenton reaction, DOX-loaded nano-MOF-treated cells have lower GSH levels as a result of the increased GSH depletion during the redox reaction with the released Fe^{III} (Fu et al. 2021; Liang et al. 2019). To sum up, after DOX-loaded nano-MOF treatment, DOX could induce to some extent elevated levels of ROS production but produce less GSH depletion, while nano-MOF not only substantially elevated the ROS production but also facilitated the GSH depletion. So, DOX-loaded nano-MOF could effectively reinforce CDT and CT efficacy. These *in-vitro* biological findings encourage the pursuit of future *in-vivo* pharmacodynamic investigation in laboratory animals.

Synthesis of ^{99m}Tc-DOX loaded AA-Fe_3O_4@Fe^{III}-TA

The radiolabeling of DOX with Tc-99m was accomplished adequately via a straightforward reductive process in which stannous chloride was incorporated to reduce the pertechnetate ($^{99m}Tc^{+7}$) to a highly reactive form ($^{99m}Tc^{+5}$) (El-Ghareb et al. 2020; Ibrahim et al. 2014; Motaleb et al. 2018). According to Fig. 6A, the radio chromatogram of ^{99m}Tc-DOX declaring the R_f values of the two mobile phases used, the radiolabeling capacity of ^{99m}Tc-DOX was estimated as ~ 96%. At room temperature, the following parameters yielded the best radiolabeling capacity: stannous chloride concentration (100 µg/mL; Fig. 6B), reaction pH (7; Fig. 6C), DOX concentration (1 mg/mL; Fig. 6D) and reaction time (30 min; Fig. 6E). The loading process of ^{99m}Tc-DOX on nano-MOF shortly after its formation exhibited a time-dependent rhythm identical to that of the non-radioactive DOX loading outlined previously. The highest loading efficiency (98%) was attained after 4 h of stirring, which is close to the recommended time for non-radioactive DOX loading.

The *in-vitro* stability experiment of ^{99m}Tc-DOX loaded nano-MOF in mice serum was evaluated since the serum protein corona's dynamic activity may change its thermodynamic and kinetic stability. Chromatographic estimates of the radiolabeling yields were made at time intervals up to 24 h in advance (Fig. 6F). It demonstrates how ^{99m}Tc-DOX loaded nano-MOF maintained an acceptable level of physiological stability for at least 8 h, 94.7%, before displaying deterioration after this point.

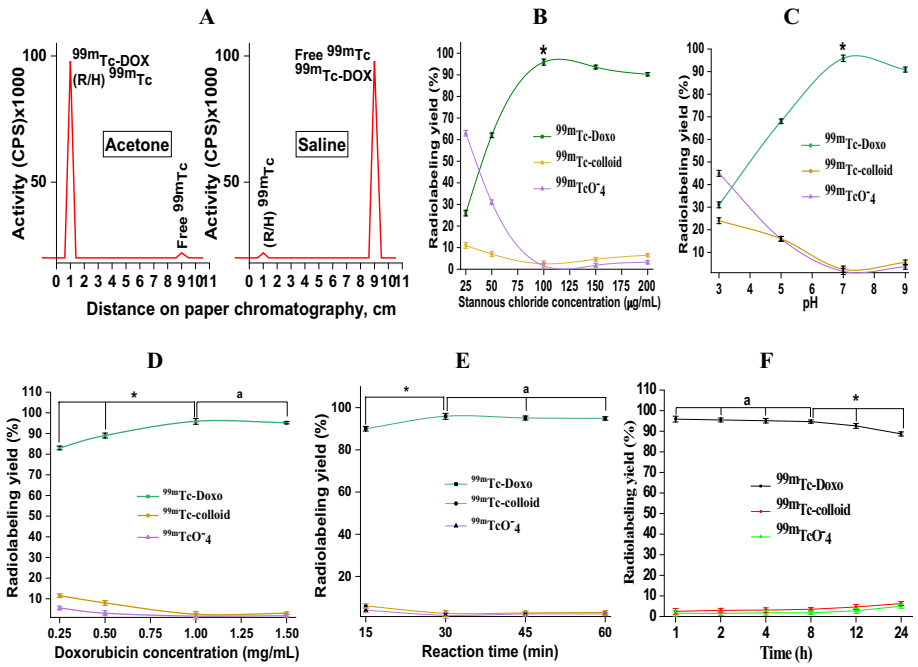

Fig. 6 The tuning profile of the radiolabeling yield percent of ^{99m}Tc-DOX. **a** Paper radio-chromatographic analysis declaring the R_f values of ^{99m}Tc-DOX in different mobile phases. **b**–**e** Factors affecting the optimization of the radiolabeling yield percent of ^{99m}Tc-DOX. **f** In-vitro stability of ^{99m}Tc-DOX over time for 24 h at 37° C in mice serum ($n = 3$). Values are expressed as "mean ± SD" (n = 3). Means were compared using ANOVA, followed by the Tukey test for multiple comparisons, two-to-two. ($^{*}p \leq 0.05$, ($^{a}p > 0.05$)

In-vivo bio-distribution studies

The *in-vivo* distribution investigations are at the forefront as a crucial strategy for figuring out the pharmacokinetic parameters associated with any newly developed nanotheranostics (Taha et al. 2023; Swidan et al. 2023). Therefore, the biodistribution pattern of ^{99m}Tc-DOX loaded nano-MOF had been explored in two different experimental groups of mice. After administering ^{99m}Tc-DOX loaded nano-MOF to normal mice intravenously, the in-vivo distribution profile demonstrated an ordinary biodistribution pattern for a nanomaterial (Fig. 7A). It displayed a satisfactory blood circulation pattern where the radioactivity was washed out and declined from 22.45 ± 1.76 to 3.2 ± 1.12% ID/g at 0.25 h and 4 h p.i., respectively. Although most organs displayed minor radioactivity buildup, the liver and spleen tissues (reticloendothelial organs) exhibited the greatest accumulation (12.17 ± 0.98 and 8.68 ± 0.47% ID/g, respectively) at 1 h p.i. Due to these organs' leaky vasculature, the considerable hepatic and splenic accumulation could potentially be addressed (Sakr et al. 2018; Swidan et al. 2019; Nie 2010). In terms of class B, the in-vivo distribution in tumor-induced mice highlighted an upward accumulation in the tumor tissues with an optimal uptake of 16.8 ± 0.88% ID/g at 1 h p.i. and declined gradually to display the lowest level of 5.8 ± 0.62% ID/g at 4 h p.i. (Fig. 7B). It's crucial to mention that this significant radioactivity level in the tumor lesion is an advancement over the naked ^{99m}Tc-DOX (only exhibited a maximum ID/g of 1.5%) (Fernandes et al. 2016). This high tumor accumulation might mainly rely on the enhanced permeability and retention (EPR) effect, which was due to the defective blood vasculature of tumor tissues, poor lymphatic drainage, and increased vessel permeability

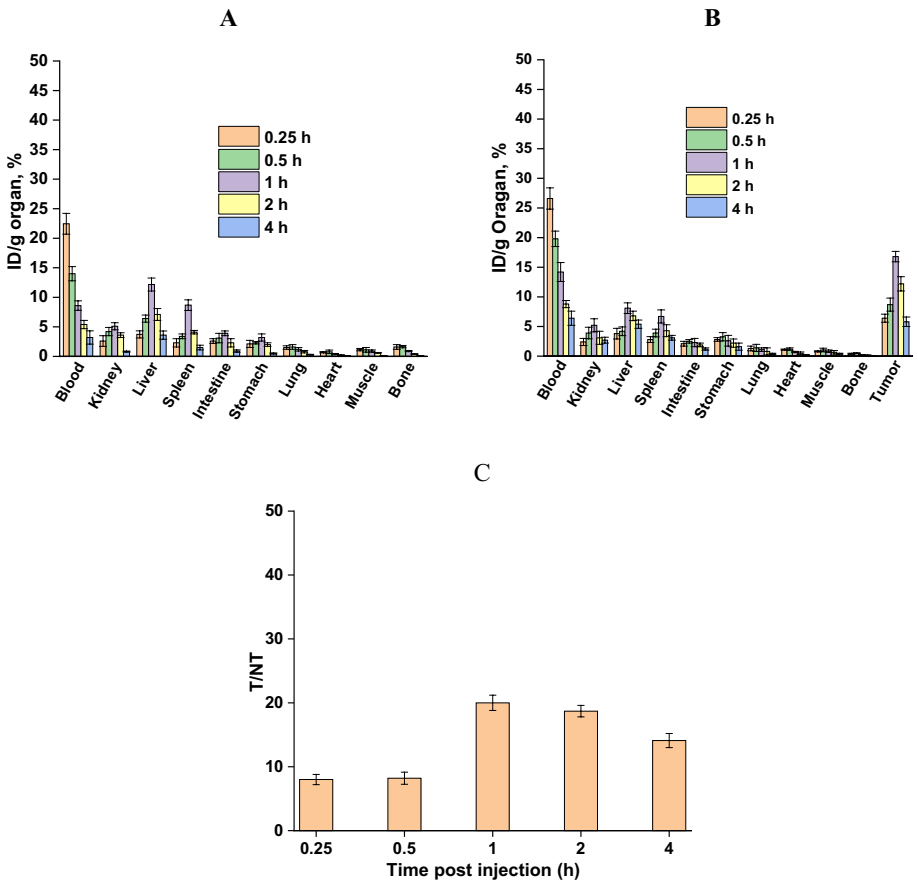

Fig. 7 In-vivo biodistribution of ^{99m}Tc-DOX loaded AA-Fe_3O_4@Fe^{III}-TA at different time intervals post i.v. administration (% ID/g ± SD): **A** normal mice **B** solid tumor-bearing mice **C** T/NT ratios as a function of time post injection. Values are expressed as "mean ± SD" ($n = 5$)

(El-Ghareb et al. 2020; Wang et al. 2020b; Kim et al. 2009). Therefore, the platform could either simultaneously target the tumor passively (small-sized nanoparticles induced EPR effect) or actively (DOX-receptor interaction) in a synergistic manner. The ability to demonstrate a considerable target accumulation (tumor lesion) in contrast to non-target (uninfected muscle), T/NT, is one of the critical obstacles in fabricating optimal radiopharmaceuticals (Mahmoud et al. 2023; El-Safoury et al. 2021a; Essa et al. 2015; El-Safoury et al. 2021b). Interestingly, Fig. 7C discovered encouraging T/NT findings along the experimental time points with a magnitude value of 8 at 1 h p.i. Herein, the considered formulation, ^{99m}Tc-Dox loaded nano-MOF, could potentially turn out as being a tumor-imaging guided SPECT tracer.

Conclusion

A unique in-situ activatable nano-MOF, ^{99m}Tc-DOX loaded AA-Fe_3O_4@Fe^{III}-TA, had been effectively engineered to operate as a tumor-selective multifunctional platform that offers improved chemo/chemodynamic theranostics. Optimized loading efficiency, pH-responsive characteristics, and nanoparticle size were all features of the biocompatible nano-MOF, which could remain stable in the bloodstream for an extended duration of time leading to enhanced tumor accumulation. The selective disintegration of

^{99m}Tc-DOX loaded AA-Fe_3O_4@Fe^{III}-TA was aided by the acidosis of the TME, which resulted in the release of TA, Fe^{III}, and the cargo ^{99m}Tc-DOX. Together, the released entities had a synergistic impact that combined SPECT imaging capabilities with a tumor-cell chemotherapeutic effect. Additionally, the burst cascade of •OH-dependent Fenton reaction increased the oxidative stress to a large degree, therefore killing tumor cells specifically. Our work offers an entirely new viewpoint on chemodynamic theranostics and shows significant promise for precise tumour treatment.

Abbreviations

•OH	Hydroxyl radicals
AA-Fe3O4 NPs	Ascorbic acid-coated iron oxide nanoparticles
CDT	Chemodynamic theranostic
CT	Chemotherapy
DDSs	Drug delivery systems
DOX	Doxorubicin
GOX	Glucose oxidase
GSH	Glutathione
ID/g	Injected Dose per Gram Organ
MB	Methylene blue
MBq	Megabecquerel
MOF	Metal organic framework
RCY	Radiochemical yield
ROS	Reactive oxygen species
T/NT	Target/non-target
TA	Tannic acid
TLC	Thin layer chromatography
TME	Tumor microenvironment

Acknowledgements
We express our gratitude to the Science, Technology & Innovation Funding Authority (STDF) in Cairo, EGYPT for their financial assistance (Applied Science Research Grants ID 46045).

Author contributions
Mohamed M. Swidan: Conceptualization, Investigation, Formal analysis, Resources, Validation, Methodology, Writing—original draft, review and editing. Nehal S. Wahba: Resources, Investigation, Methodology, Formal analysis, Writing—original draft, review and editing. Tamer M. Sakr: Conceptualization, Resources, Supervision, Funding acquisition, Writing—review and editing.

Funding
Open access funding provided by The Science, Technology & Innovation Funding Authority (STDF) in cooperation with The Egyptian Knowledge Bank (EKB).

Availability of data and materials
This article contains all of the data that was generated or investigated during the course of this research.

Declarations

Ethics approval and consent to participate
All animal procedures were carried out in compliance with the research ethics committee for experimental studies (Human & Animal subject) at National center for research radiation and technology - Egyptian Atomic Energy Authority (REC-NCRRT-EAEA) under clearance No 19PA/23. This committee is following the 3Rs principles for animal experimentation and is organized and operated according to the CIOMS and ICLAS International Guiding Principles for Biomedical Research Involving Animals 2012.

Consent for publication
All authors contributed to the writing of the manuscript where its final version was approved by all of them.

Competing of interests
All authors declare no competing interests.

Received: 28 April 2024 Accepted: 24 May 2024
Published online: 12 June 2024

References
Ajaykumar C. (2020) Overview on the side effects of doxorubicin. Advances in Precision Medicine Oncology

An J, Hu Y-G, Cheng K, Li C, Hou X-L, Wang G-L et al (2020) ROS-augmented and tumor-microenvironment responsive biodegradable nanoplatform for enhancing chemo-sonodynamic therapy. Biomaterials 234:119761
Asefi Y, Fahimi R, Ghorbian S (2021) Synergistic effect of vitamin c with superparamagnetic iron oxide nanoparticles for inhibiting proliferation of gastric cancer cells. Biointerfaces Res Appl Chem 12:3215–3224
Chen X, Zhang H, Zhang M, Zhao P, Song R, Gong T et al (2020) Amorphous Fe-based nanoagents for self-enhanced chemodynamic therapy by re-establishing tumor acidosis. Adv Func Mater 30(6):1908365
Chen F, Yang B, Xu L, Yang J, Li J (2021) A CaO2@ tannic acid-feiii nanoconjugate for enhanced chemodynamic tumor therapy. ChemMedChem 16(14):2278–2286
Chen X, Wang L, Liu S, Luo X, Wang K, He Q (2022a) Cisplatin-loaded metal–phenolic network with photothermal-triggered ROS generation for chemo-photothermal therapy of cancer. Cancer Nanotechnol 13(1):41
Chen C, Yang H, Yang X, Ma Q (2022b) Tannic acid: a crosslinker leading to versatile functional polymeric networks: a review. RSC Adv 12(13):7689–7711
Cui R, Shi J, Liu Z (2021) Metal–organic framework-encapsulated nanoparticles for synergetic chemo/chemodynamic therapy with targeted H2O2 self-supply. Dalton Trans 50(43):15870–15877
Dai Y, Yang Z, Cheng S, Wang Z, Zhang R, Zhu G et al (2018) Toxic reactive oxygen species enhanced synergistic combination therapy by self-assembled metal-phenolic network nanoparticles. Adv Mater 30(8):1704877
Deng S, Kruger A, Kleschyov AL, Kalinowski L, Daiber A, Wojnowski L (2007) Gp91phox-containing NAD (P) H oxidase increases superoxide formation by doxorubicin and NADPH. Free Radic Biol Med 42(4):466–473
Ding B, Shao S, Jiang F, Dang P, Sun C, Huang S et al (2019) MnO2-disguised upconversion hybrid nanocomposite: an ideal architecture for tumor microenvironment-triggered UCL/MR bioimaging and enhanced chemodynamic therapy. Chem Mater 31(7):2651–2660
Ding Y, Xu H, Xu C, Tong Z, Zhang S, Bai Y et al (2020) A nanomedicine fabricated from gold nanoparticles-decorated metal-organic framework for cascade chemo/chemodynamic cancer therapy. Advanced Science 7(17):2001060
Ejima H, Richardson JJ, Liang K, Best JP, van Koeverden MP, Such GK et al (2013) One-step assembly of coordination complexes for versatile film and particle engineering. Science 341(6142):154–157
El-Ghareb WI, Swidan MM, Ibrahim IT, Abd El-Bary A, Tadros MI, Sakr TM (2020) 99mTc-Doxorubicin-loaded gallic acid-gold nanoparticles (99mTc-DOX-loaded GA-Au NPs) as a multifunctional theranostic agent. Int J Pharm 586:119514
El-Safoury D, Ibrahim AB, El-Setouhy D, Khowessah O, Motaleb M, Sakr TM (2021a) Gold nanoparticles for 99m Tc-doxorubicin delivery: formulation, in vitro characterization, comparative studies in vivo stability and biodistribution. J Radioanal Nucl Chem 328(1):325–338
El-Safoury D, Ibrahim AB, El-Setouhy D, Khowessah O, Motaleb M, Sakr TM (2021b) Amelioration of tumor targeting and in vivo biodistribution of 99mtc-methotrexate-gold Nanoparticles (99mTc-Mex-AuNPs). J Pharm Sci 110(8):2955–2965
Essa B, Sakr T, Khedr MA, El-Essawy F, El-Mohty A (2015) 99mTc-amitrole as a novel selective imaging probe for solid tumor: in silico and preclinical pharmacological study. Eur J Pharm Sci 76:102–109
Feng W, Han X, Wang R, Gao X, Hu P, Yue W et al (2019) Nanocatalysts-augmented and photothermal-enhanced tumor-specific sequential nanocatalytic therapy in both NIR-I and NIR-II biowindows. Adv Mater 31(5):1805919
Fernandes RS, de Oliveira SJ, Lopes SC, Chondrogiannis S, Rubello D, Cardoso VN et al (2016) Technetium-99m-labeled doxorubicin as an imaging probe for murine breast tumor (4T1 cell line) identification. Nucl Med Commun 37(3):307–312
Fu LH, Wan Y, Qi C, He J, Li C, Yang C et al (2021) Nanocatalytic theranostics with glutathione depletion and enhanced reactive oxygen species generation for efficient cancer therapy. Adv Mater 33(7):2006892
Fukumura H, Sato M, Kezuka K, Sato I, Feng X, Okumura S et al (2012) Effect of ascorbic acid on reactive oxygen species production in chemotherapy and hyperthermia in prostate cancer cells. J Physiol Sci 62(3):251–257
Gao S, Jin Y, Ge K, Li Z, Liu H, Dai X et al (2019) Self-supply of O2 and H2O2 by a Nanocatalytic medicine to enhance combined chemo/Chemodynamic therapy. Adv Sci 6(24):1902137
Gu D, An P, He X, Wu H, Gao Z, Li Y et al (2020) A novel versatile yolk-shell nanosystem based on NIR-elevated drug release and GSH depletion-enhanced Fenton-like reaction for synergistic cancer therapy. Colloids Surf, B 189:110810
Guo Y, Zhang X, Sun W, Jia H-R, Zhu Y-X, Zhang X et al (2019) Metal–phenolic network-based nanocomplexes that evoke ferroptosis by apoptosis: promoted nuclear drug influx and reversed drug resistance of cancer. Chem Mater 31(24):10071–10084
Guo Y, Jia HR, Zhang X, Zhang X, Sun Q, Wang SZ et al (2020) A glucose/oxygen-exhausting nanoreactor for starvation-and hypoxia-activated sustainable and cascade chemo-chemodynamic therapy. Small 16(31):2000897
Han Y, Ouyang J, Li Y, Wang F, Jiang J-H (2019) Engineering H2O2 self-supplying nanotheranostic platform for targeted and imaging-guided chemodynamic therapy. ACS Appl Mater Interf 12(1):288–297
Hernandes EP, Lazarin-Bidóia D, Bini RD, Nakamura CV, Cótica LF (2023) Doxorubicin-loaded iron oxide nanoparticles induce oxidative stress and cell cycle arrest in breast cancer cells. Antioxidants 12(2):237
Huang L, Jiang S, Cai B, Wang G, Wang Z, Wang L (2021) pH-Triggered nanoreactors as oxidative stress amplifiers for combating multidrug-resistant biofilms. Chem Commun 57(38):4662–4665
Ibrahim A, Sakr T, Khoweysa O, Motaleb M, Abd El-Bary A, El-Kolaly M (2014) Formulation and preclinical evaluation of 99m Tc–gemcitabine as a novel radiopharmaceutical for solid tumor imaging. J Radioanal Nucl Chem 302:179–186
Kim H-S, Lee Y-S, Kim D-K (2009) Doxorubicin exerts cytotoxic effects through cell cycle arrest and Fas-mediated cell death. Pharmacology 84(5):300–309
Korany M, Marzook F, Mahmoud B, Ahmed SA, Ayoub SM, Sakr TM (2020) Exhibiting the diagnostic face of selenium nanoparticles as a radio-platform for tumor imaging. Bioorg Chem 100:103910
Lei M, Chen G, Zhang M, Lei J, Li T, Li D et al (2021) A pH-sensitive drug delivery system based on hyaluronic acid co-deliver doxorubicin and aminoferrocene for the combined application of chemotherapy and chemodynamic therapy. Colloids Surf, B 203:111750

Li Z, Wu X, Wang W, Gai C, Zhang W, Li W et al (2021) Fe (II) and tannic acid-cloaked MOF as carrier of artemisinin for supply of ferrous ions to enhance treatment of triple-negative breast cancer. Nanoscale Res Lett 16:1–11
Li H, Zhang Y, Liang L, Song J, Wei Z, Yang S et al (2022) Doxorubicin-loaded metal-organic framework nanoparticles as acid-activatable hydroxyl radical nanogenerators for enhanced chemo/chemodynamic synergistic therapy. Materials 15(3):1096
Liang R, Chen Y, Huo M, Zhang J, Li Y (2019) Sequential catalytic nanomedicine augments synergistic chemodrug and chemodynamic cancer therapy. Nanoscale Horizons 4(4):890–901
Lin LS, Song J, Song L, Ke K, Liu Y, Zhou Z et al (2018) Simultaneous Fenton-like ion delivery and glutathione depletion by MnO2-based nanoagent to enhance chemodynamic therapy. Angew Chem 130(18):4996–5000
Lin L-S, Huang T, Song J, Ou X-Y, Wang Z, Deng H et al (2019) Synthesis of copper peroxide nanodots for H2O2 self-supplying chemodynamic therapy. J Am Chem Soc 141(25):9937–9945
Liu Y, Ji X, Tong WW, Askhatova D, Yang T, Cheng H et al (2018) Engineering multifunctional RNAi nanomedicine to concurrently target cancer hallmarks for combinatorial therapy. Angew Chem 130(6):1526–1529
Liu P, Xie X, Shi X, Peng Y, Ding J, Zhou W (2019) Oxygen-self-supplying and HIF-1α-inhibiting core–shell nanosystem for hypoxia-resistant photodynamic therapy. ACS Appl Mater Interfaces 11(51):48261–48270
Liu X, Jin Y, Liu T, Yang S, Zhou M, Wang W et al (2020a) Iron-based theranostic nanoplatform for improving chemodynamic therapy of cancer. ACS Biomater Sci Eng 6(9):4834–4845
Liu C, Cao Y, Cheng Y, Wang D, Xu T, Su L et al (2020b) An open source and reduce expenditure ROS generation strategy for chemodynamic/photodynamic synergistic therapy. Nat Commun 11(1):1735
Ma B, Wang S, Liu F, Zhang S, Duan J, Li Z et al (2018) Self-assembled copper–amino acid nanoparticles for in situ glutathione "AND" H2O2 sequentially triggered chemodynamic therapy. J Am Chem Soc 141(2):849–857
Mahmoud AF, Aboumanei MH, Abd-Allah WH, Swidan MM, Sakr TM (2023) New frontier radioiodinated probe based on in silico resveratrol repositioning for microtubules dynamic targeting. Int J Radiat Biol 99(2):281–291
Mizutani H, Tada-Oikawa S, Hiraku Y, Kojima M, Kawanishi S (2005) Mechanism of apoptosis induced by doxorubicin through the generation of hydrogen peroxide. Life Sci 76(13):1439–1453
Motaleb MA, El-Safoury DM, Abd-Alla WH, Awad GA, Sakr TM (2018) Radiosynthesis, molecular modeling studies and biological evaluation of 99mTc-Ifosfamide complex as a novel probe for solid tumor imaging. Int J Radiat Biol 94(12):1134–1141
Nie S (2010) Understanding and overcoming major barriers in cancer nanomedicine. Nanomedicine 5(4):523–528
Nie Y, Li D, Peng Y, Wang S, Hu S, Liu M et al (2020) Metal organic framework coated MnO2 nanosheets delivering doxorubicin and self-activated DNAzyme for chemo-gene combinatorial treatment of cancer. Int J Pharm 585:119513
Ozel F, Tokay E, Köçkar F, Köçkar H (2018) Characterization of tartaric acid and ascorbic acid coated iron oxide nanoparticles and their biocompatibility studies. J Magn Magn Mater 474:654–660
Özel F, Karaagac O, Tokay E, Köçkar F, Köçkar H (2019) A simple way to synthesize tartaric acid, ascorbic acid and their mixture coated superparamagnetic iron oxide nanoparticles with high saturation magnetisation and high stability against oxidation: characterizations and their biocompatibility studies. J Magn Magn Mater 474:654–660
Sakr TM, Khowessah O, Motaleb M, Abd El-Bary A, El-Kolaly M, Swidan MM (2018) I-131 doping of silver nanoparticles platform for tumor theranosis guided drug delivery. Eur J Pharm Sci 122:239–245
Shagholani H, Ghoreishi SM (2017) Investigation of tannic acid cross-linked onto magnetite nanoparticles for applying in drug delivery systems. J Drug Delivery Sci Technol 39:88–94
Shi L, Wang Y, Zhang C, Zhao Y, Lu C, Yin B et al (2021) An acidity-unlocked magnetic nanoplatform enables self-boosting ROS generation through upregulation of lactate for imaging-guided highly specific chemodynamic therapy. Angew Chem 133(17):9648–9658
Sreeja V, Jayaprabha K, Joy P (2015) Water-dispersible ascorbic-acid-coated magnetite nanoparticles for contrast enhancement in MRI. Appl Nanosci 5:435–441
Swidan MM, Khowessah OM, El-Motaleb MA, El-Bary AA, El-Kolaly MT, Sakr TM (2019) Iron oxide nanoparticulate system as a cornerstone in the effective delivery of Tc-99 m radionuclide: a potential molecular imaging probe for tumor diagnosis. DARU J Pharm Sci 27:49–58
Swidan MM, Abd El-Motaleb M, Sakr TM (2022) Unraveling the diagnostic phase of 99mTc-doped iron oxide nanoprobe in sarcoma bearing mice. J Drug Delivery Sci Technol 78:103990
Swidan MM, Essa BM, Sakr TM (2023) Pristine/folate-functionalized graphene oxide as two intrinsically radioiodinated nano-theranostics: self/dual in vivo targeting comparative study. Cancer Nanotechnol 14(1):1–17
Taha E, Nour SA, Mamdouh W, Selim AA, Swidan MM, Ibrahim AB et al (2023) Cod liver oil nano-structured lipid carriers (Cod-NLCs) as a promising platform for nose to brain delivery: preparation, in vitro optimization, ex vivo cytotoxicity & in vivo biodistribution utilizing radioiodinated zopiclone. Int J Pharm x 5:100160
Tang Z, Liu Y, He M, Bu W (2019) Chemodynamic therapy: tumour microenvironment-mediated Fenton and Fenton-like reactions. Angew Chem 131(4):958–968
Thorn CF, Oshiro C, Marsh S, Hernandez-Boussard T, McLeod H, Klein TE et al (2011) Doxorubicin pathways: pharmacodynamics and adverse effects. Pharmacog Genom 21(7):440
Ubezio P, Civoli F (1994) Flow cytometric detection of hydrogen peroxide production induced by doxorubicin in cancer cells. Free Radic Biol Med 16(4):509–516
Wagner BA, Evig CB, Reszka KJ, Buettner GR, Burns CP (2005) Doxorubicin increases intracellular hydrogen peroxide in PC3 prostate cancer cells. Arch Biochem Biophys 440(2):181–190
Wang X-G, Dong Z-Y, Cheng H, Wan S-S, Chen W-H, Zou M-Z et al (2015) A multifunctional metal–organic framework based tumor targeting drug delivery system for cancer therapy. Nanoscale 7(38):16061–16070
Wang Y, Liu Y, Xu J (2019) Separation of hydrogen sulfide from gas phase using Ce3+/Mn2+-enhanced fenton-like oxidation system. Chem Eng J 359:1486–1492
Wang T, Zhang H, Liu H, Yuan Q, Ren F, Han Y et al (2020a) Boosting h2o2-guided chemodynamic therapy of cancer by enhancing reaction kinetics through versatile biomimetic fenton nanocatalysts and the second near-infrared light irradiation. Adv Func Mater 30(3):1906128

Wang S-Y, Hu H-Z, Qing X-C, Zhang Z-C, Shao Z-W (2020b) Recent advances of drug delivery nanocarriers in osteosarcoma treatment. J Cancer 11(1):69
Wang N, Liu C, Yao W, Zhou H, Yu S, Chen H et al (2021a) A traceable, sequential multistage-targeting nanoparticles combining chemo/chemodynamic therapy for enhancing antitumor efficacy. Adv Func Mater 31(26):2101432
Wang N, Zeng Q, Zhang R, Xing D, Zhang T (2021b) Eradication of solid tumors by chemodynamic theranostics with H2O2-catalyzed hydroxyl radical burst. Theranostics 11(5):2334
Zhang L, Wan S-S, Li C-X, Xu L, Cheng H, Zhang X-Z (2018) An adenosine triphosphate-responsive autocatalytic fenton nanoparticle for tumor ablation with self-supplied H2O2 and acceleration of Fe (III)/Fe (II) conversion. Nano Lett 18(12):7609–7618
Zheng Y, Qin C, Li F, Qi J, Chu X, Li H et al (2023) Self-assembled thioether-bridged paclitaxel-dihydroartemisinin prodrug for amplified antitumor efficacy-based cancer ferroptotic-chemotherapy. Biomater Sci 11(9):3321–3334

Publisher's Note